

Research Article

In situ grown Bi₂S₃ nanorods in Cs₃Bi₂I₉ thin films as broadband self-driven photodetector with improved photostability

Sebin Devasia ^{a,1}, Sadasivan Shaji ^{a,b}, David Avellaneda Avellaneda ^a, Josue Amilcar Aguilar Martinez ^{a,c}, Bindu Krishnan ^{a,b,*}

^a Facultad de Ingeniería Mecánica y Eléctrica, Universidad Autónoma de Nuevo León, San Nicolás de los Garza, Nuevo León, 66455, Mexico

^b Centro de Innovación, Investigación y Desarrollo en Ingeniería y Tecnología (CIIDIT)- Universidad Autónoma de Nuevo León, Parque de Investigación e Innovación Tecnológica (PIIT), Apodaca, Nuevo León, 66600, Mexico

^c Centro de Investigación e Innovación en Ingeniería Aeronáutica (CIIIA), Facultad de Ingeniería Mecánica y Eléctrica, Carretera a Salinas Victoria, Apodaca, Nuevo León, 66600, Mexico

ARTICLE INFO

Keywords:

Lead-free perovskite
Cs₃Bi₂I₉ thin films
Bi₂S₃ nanorods
Ultra sonic spray deposition
Zero biased photodetector

ABSTRACT

This study reports *in-situ* growth of bismuth sulfide (Bi₂S₃) nanorods incorporated cesium bismuth iodide (Cs₃Bi₂I₉) thin films with improved photostability using a single-step ultrasonic spray deposition. The spray deposition was done using a non-aqueous solution containing CsI (0.0025 M), BiI₃ (0.005 M), and thioacetamide in acetone, by varying concentrations of thioacetamide (0.005, 0.009, 0.01, 0.03 and 0.05 M) and the substrate temperature was 200 °C. The structure, morphology, and composition analysis of the films showed the formation of Cs₃Bi₂I₉ thin films decorated with vertically aligned Bi₂S₃ nanorods in the intergranular region. The *in situ*-grown Cs₃Bi₂I₉:Bi₂S₃ composite thin films were photosensitive and photostable. The photodiode of FTO/CdS/Cs₃Bi₂I₉:Bi₂S₃/C-Ag demonstrated a stable spectral response for a wide wavelength range (405–1064 nm), with a detectivity of 8.18×10^9 Jones and responsivity of 0.59 mAW⁻¹ under 532 nm illumination, operating in self-driven mode.

1. Introduction

In search for a potential replacement for Pb-based perovskites, Cs₃Bi₂I₉ perovskite-derived semiconductor has found excellent applications in photon and harmful hard radiation detectors [1–3]. Cs₃Bi₂I₉ has also shown applications in photovoltaics [4], piezoelectric nanogenerators [5], electrode material for supercapacitors [6], integrated photobattery [7], and photocatalysis [8,9]. Recently, Cs₃Bi₂I₉ has gained special attention due to its self-driven photodetection which eliminates the need for an external power supply to drive the photo-generated charge carriers in the photosensor device [10].

Cesium bismuth iodide thin films have been fabricated mostly by spin coating of DMF or DMSO based precursor solution [3,11–14]. The spin coated Cs₃Bi₂I₉ thin films showed self-powered photodetection with detectivities up to $\sim 10^{11}$ Jones and responsivities as high as 15×10^{-3} AW⁻¹ [13]. Besides, space-limited methods were employed to grow Cs₃Bi₂I₉ single crystals with excellent photodetection properties [10,15,16]. Recently, our research group has shown that ultrasonic spray

deposition can be used for the *in situ* formation of lead-free halide Cs₃Bi₂I₉ thin films using non-toxic ethanol for photodetection applications. Even a low-concentration precursor solution can be used here, resulting in minimal material loss during the deposition compared to other solution-based methods such as spin-coating [17]. Ultrasonic spray deposition is done under ambient conditions indicating an excellent opportunity for scaling up the process. This solution-based technique facilitates various aspects of solution engineering such as doping, solvent modifications to control crystallization, and thin film growth on selected areas including non-planar surfaces. The controlled substrate temperature enables the growth of multiple phases or bulk heterojunction devices [18,19]. These advantages prompted the use of spray deposition over conventional deposition techniques for perovskite-based optoelectronics [20].

Extracting photocarriers by incorporating nanostructures into the bulk absorber layer can be a promising technique to enhance the photodetector device performance [21–23]. Methyl ammonium lead iodide perovskite deposited on the gradient O-doped CdS nanorods

* Corresponding author. Facultad de Ingeniería Mecánica y Eléctrica, Universidad Autónoma de Nuevo León, San Nicolás de los Garza, Nuevo León, 66455, Mexico.

E-mail addresses: krishnan.bindu@uanl.edu.mx, kbbindu_k@yahoo.com (B. Krishnan).

¹ Current Affiliation: PSG Institute of Advanced Studies, Avinashi Road, Peelamedu, Coimbatore, 641004, India.

induced excellent detectivity of 2.1×10^{13} Jones with a high responsivity of 0.48 AW^{-1} and a rise/decay time of $0.54/2.21 \text{ ms}$ [24].

Herein, we synthesize composite thin films of Bi_2S_3 nanorods incorporated $\text{Cs}_3\text{Bi}_2\text{I}_9$ to enhance the charge collection in photodetectors. Ultrasonically spraying acetone-based precursor solution containing CsI , BiI_3 , and thioacetamide leads to the growth of $\text{Cs}_3\text{Bi}_2\text{I}_9$ grains with Bi_2S_3 nanorods at the boundaries. Detailed investigations of the structure, morphology, optical, and electrical properties of these composite films suggest improved charge collection and photostability. These findings motivated the design of self-powered photodetectors. Interestingly, these devices show better performance in a broad spectral range compared to that of the controlled device using pure $\text{Cs}_3\text{Bi}_2\text{I}_9$ thin films. The solution-based ultrasonic spray deposition technique allows the growth of such phase-separated composite films in a single step over large areas by fine-tuning the composition of constituent components in the precursor solution.

2. Materials and methods

2.1. $\text{Cs}_3\text{Bi}_2\text{I}_9:\text{Bi}_2\text{S}_3$ composite thin film deposition

590 mg of bismuth iodide (BiI_3 , laboratory synthesized) and 130 mg of cesium iodide (CsI , Aldrich, 99.9 %) were dissolved in 200 ml acetone by stirring for 2 h at 60°C . Thioacetamide (CH_3CSNH_2 , Sigma Aldrich, >99.0 %) was added to the same solution as the sulfur source. Precursor solutions with different concentrations of thioacetamide as 0.005, 0.01, 0.03 and 0.05 M were prepared. The ultrasonic spray deposition technique (Equipment: Zhengzhou Tainuo Film Materials Co., Ltd.) was used to deposit thin films from these precursor solutions. The pure $\text{Cs}_3\text{Bi}_2\text{I}_9$ film prepared without thioacetamide adding to the precursor was labelled as pCBI. The samples formed at different concentrations of thioacetamide were marked as TA05, TA1, TA3 and TA5, respectively. For thioacetamide molarity higher than 0.05, the composite films were powdery and there was no improvement in the optoelectronic properties. Therefore we did not proceed with further increase in concentration of thioacetamide. The deposition was done at 200°C substrate temperature for 1 ml/min spray rate. The precursor solution was sprayed onto an area of $150 \times 150 \text{ mm}^2$ using x- and y-axis movements of the ultrasonic nozzle (40 kHz, 130 W) with the help of stepper motors. The nozzle covered this area 120 times to achieve sufficient thickness. To check the thermal stability, the thin films were annealed at 200, 300, 350 and 400°C for 30 min in the low vacuum furnace maintaining a vacuum of $\sim 10^{-2}$ Torr (VBF-1200X, MTI corporation). Pure Bi_2S_3 thin films were also grown for comparison, using 0.005 M BiCl_3 and thioacetamide of 0.04 M. The choice of BiCl_3 molarity was in correlation with that of BiI_3 and the molarity of thioacetamide was eight times by considering the high volatility of sulfur.

2.2. Fabrication of photodiode

Initially, the CdS layer was deposited on a cleaned FTO substrate by chemical bath deposition as reported elsewhere [25]. Further, pCBI (pure $\text{Cs}_3\text{Bi}_2\text{I}_9$ film prepared without thioacetamide) or TA3 films were spray deposited on the CdS layer with proper masking at 200°C [17,26]. Finally, carbon and silver painted electrodes resulting in glass-/FTO/ CdS /pCBI and TA3/C-Ag heterostructure devices.

2.3. Characterization

The structural properties of the thin films were analyzed using the X-ray diffraction (XRD) patterns obtained using a PANalytical EMPYREAN diffractometer with $\text{Cu K}\alpha$ radiation ($\lambda = 1.5406 \text{ \AA}$) and the Raman spectra collected from a Thermo Scientific DXR Raman microscope with 532 nm excitation wavelength. The scanning electron microscopy (SEM) images taken by a SU8020 HITACHI microscope were used to probe the morphology and thickness of the thin films. The elemental states and

chemical composition of the thin films were analyzed by X-ray photoelectron spectroscopy (XPS). The samples were kept in the parking chamber for 18 h under a vacuum of 1×10^{-6} mbar before moving to the analysis chamber. The calibration and linearity of the binding energy scale were confirmed using $\text{Ag } 3\text{d}_{5/2}$ peak with FWHM of 0.9 eV, recorded from a silver foil kept inside the spectrometer by the manufacturer. A flood gun with low-energy electrons was used for charge compensation. The spectra recorded include the survey (pass energy 200 eV) as well as high resolution (pass energy 50 eV). The spectra were recorded after one cycle of Ar^+ etching. Though a flood gun is used in the measurements for charge compensation, any charging effect was further corrected using the adventitious carbon (C 1s) peak energy at 284.6 eV [27]. During XPS spectra acquisition, the base pressure in the analysis chamber was 1×10^{-9} mBar achieved using a titanium sublimation pump in combination with two 260 l/s turbo molecular pump systems. The X-ray source was $\text{AlK}\alpha$ (Energy: 1486.68 eV, Voltage: 12 kV, Current: $3 \times 10^{-3} \text{ A}$) with a micro-focused X-ray monochromator and the analysis area was that of the focused X-ray beam spot size of 400 μm . B.E values of the photoelectrons were analyzed using a 180° double-focusing hemispherical analyzer (CAE mode; work function 4.2 eV) with a 128-channel electron detector. Depth profiling of composition was performed by etching the sample surface using an Ar^+ ion gun (2 keV energy incident with an inclination of 30°) at a sputtering rate of 1.22/s.

The absorption of the thin films in the 300–1200 nm spectral range was measured using a JASCO UV-Vis-NIR spectrophotometer. A Keithley 6487 picoammeter was used to measure the self-driven transient photoresponse of the thin films and devices to AM1.5 illumination. Further, the photodetection performance of the device was evaluated under various lasers of wavelengths such as 405, 532, 785, 840, 980 and 1064 nm.

3. Results and discussion

3.1. Crystal structure

The powder X-ray diffraction patterns in Fig. 1a of the thin films show only peaks corresponding to hexagonal polycrystalline $\text{Cs}_3\text{Bi}_2\text{I}_9$ ($\text{P}6_3/\text{mmc}$), similar to the pure $\text{Cs}_3\text{Bi}_2\text{I}_9$ (pCBI) thin films matching with the ICDD file 01-073-0707. From the figure, we can see (006) oriented growth in pCBI and the films formed using lower thioacetamide (TA) concentrations (TA05 and TA1). Noticeably, the crystalline nature changes in the TA3 and TA5 thin films as different planes grow at the expense of (006) oriented crystallites. The texture coefficients corresponding to the (006) and (101) planes were calculated [28]. The TC_{006} increases from 2.68 for pCBI to 3.87 for TA1 and then decreases to 2.65 and 2.49 for TA3 and TA5, respectively. At the same time, TC_{101} increases from 0.19 to 0.84 with thioacetamide concentration. Though the increase in sulfur content in the precursor solution improves the (006) oriented crystallization of $\text{Cs}_3\text{Bi}_2\text{I}_9$ at lower thioacetamide concentrations, higher concentrations of sulfur appear to limit this growth as seen in TA3 and TA5 films. On the other hand, (101) and (202) peaks grow stronger implying sulfur-induced crystallite growth along different directions. Further, even in TA5 films, there is no evidence of any peak corresponding to the presence of Bi_2S_3 .

The average crystallite size calculated from XRD patterns using the respective W-H plots is given in Table 1. The crystallite size increases and the strain decreases with thioacetamide addition. The improved crystallite size of $\text{Cs}_3\text{Bi}_2\text{I}_9$ can be due to the growth of the film favored by the Bi_2S_3 nanostructures as the nucleation sites [29].

Highly oriented $\text{Cs}_3\text{Bi}_2\text{I}_9$ thin film growth along (006) with large crystallite size is normally reported, from precursor solutions containing BiI_3 and CsI [3,11–14,30]. Further, the formations of single crystals and devices are also known [10,15,16]. In our case, thin films with crystallite size 47–55 nm were grown with orientation varied from (006) to random by in-situ incorporation of Bi_2S_3 nanorods.

For further analysis of the composite thin films, the diffraction

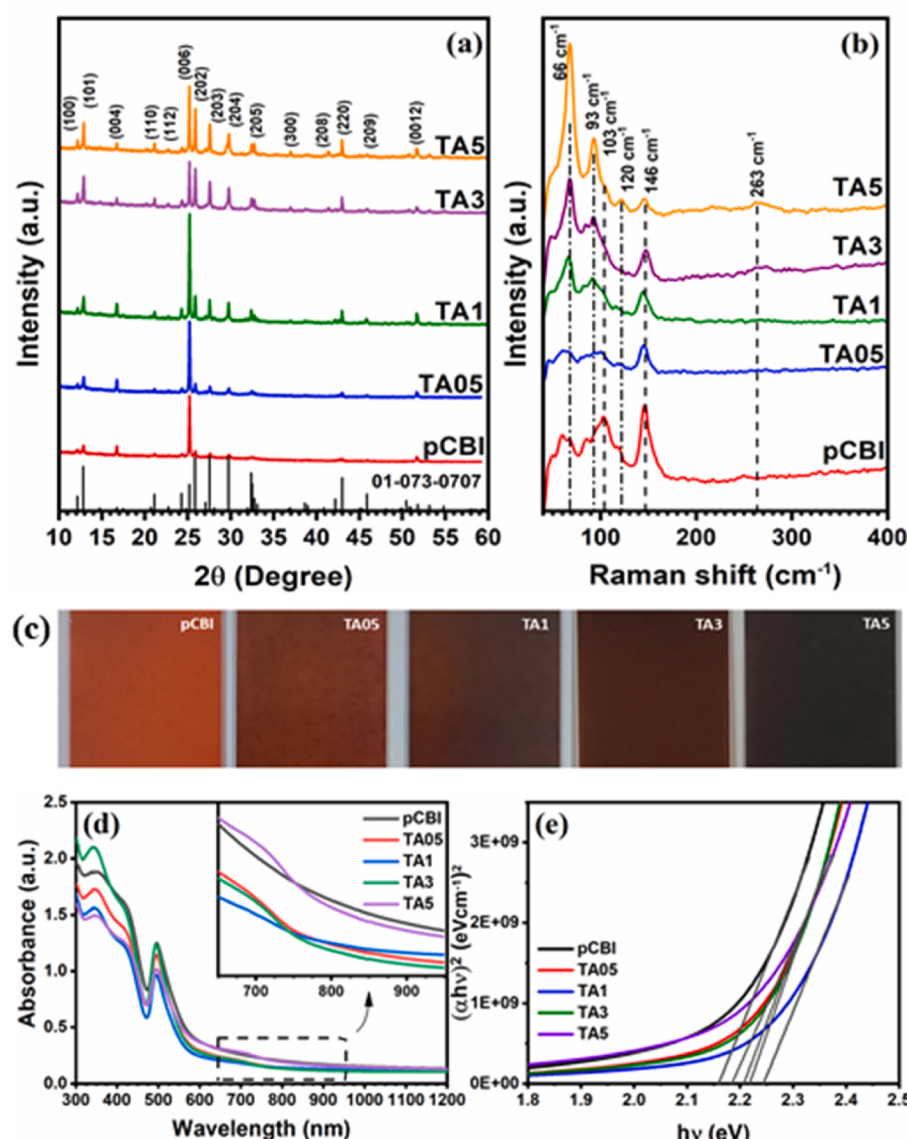


Fig. 1. (a) The X-ray diffraction patterns (b) Raman spectra of the pure $\text{Cs}_3\text{Bi}_2\text{I}_9$ and $\text{Cs}_3\text{Bi}_2\text{I}_9:\text{Bi}_2\text{S}_3$ composite thin films (c) Pure $\text{Cs}_3\text{Bi}_2\text{I}_9$ (pCBI) and $\text{Cs}_3\text{Bi}_2\text{I}_9:\text{Bi}_2\text{S}_3$ (TA) composite thin films with different thioacetamide concentrations (thin film area $2.5 \text{ cm} \times 2.5 \text{ cm}$) (d) The absorbance spectra (e) Tauc plots to evaluate bandgaps from the pCBI and composite thin films.

Table 1
Quantitative analysis of XRD and SEM results.

Sample	W-H plot		SEM images		
	Average crystallite size (nm)	Strain ($\times 10^{-4}$)	Avg. Grain size (nm)	Bi_2S_3 nanorods	
				Length (nm)	Diameter (nm)
pCBI	47.8	7.5	301.7	–	–
TA05	47.8	1.5	382.5	67	50
TA1	57.8	3.8	343.9	120	80
TA3	51.4	1.8	268.4	177	83
TA5	55.5	2.3	439.4	288	122

patterns of the spray-deposited Bi_2S_3 thin film at similar spray parameters are discussed in the supplementary material. The diffraction pattern given in S1a shows poor crystallinity with very low intense peaks [31–33]. In the XRD patterns of $\text{Cs}_3\text{Bi}_2\text{I}_9:\text{Bi}_2\text{S}_3$ thin films, the peaks corresponding to Bi_2S_3 are too low in intensity to be distinguishable from the much stronger peaks of $\text{Cs}_3\text{Bi}_2\text{I}_9$. However, the

Raman spectra of the thin films in Fig. 1b show an additional peak at 263 cm^{-1} compared to that of pCBI which is attributed to the B_1 vibration in Bi_2S_3 as seen in S1b [32]. The other peaks near 62, 104, and 146 cm^{-1} are associated with the $\text{Cs}_3\text{Bi}_2\text{I}_9$ structure [26]. The low-frequency Raman line close to 62 cm^{-1} is associated with the vibrations of $[\text{Bi}_2\text{I}_9]^{3-}$ biotahedral units with A_1^+ symmetry. The peak near 104 cm^{-1} is a result of $[\text{Bi}_6]^{3-}$ vibrations inside this biotahedra. The prominent peak in pCBI at 146 cm^{-1} is attributed to the vibrational modes of Bi-I bonds [31,34,35].

Photographs of pure and bismuth sulfide integrated thin films are presented in Fig. 1c. The color change from red-brown to black is due to absorption in the wavelength region (700–900 nm) arising from the vertically aligned Bi_2S_3 nanorods, as shown in Fig. 1d. The Bi_2S_3 nanorod incorporated films are darker as thioacetamide concentration in the precursor solution increases. Since the film's phase remains unchanged with the increase in the thioacetamide concentration, we attribute the darker appearance of the thin films to the growth of Bi_2S_3 , which is black because of its low bandgap of approximately 1.4 eV (S1). Also, a photograph of the sprayed Bi_2S_3 thin film is included in S1. Thus, by comparing the morphologies of pure Bi_2S_3 , $\text{Cs}_3\text{Bi}_2\text{I}_9$, and Bi_2S_3 nanorod

incorporated $\text{Cs}_3\text{Bi}_2\text{I}_9$ thin films, the black color of the composite thin films can originate from the surface nonuniformity by the growth of Bi_2S_3 nanorods. The details of optical absorption are discussed in optical properties (3.5). The optical absorption of pure Bi_2S_3 thin film is given in S1.

3.2. Morphology

The morphology of the pCBI and composite thin films is given in Fig. 2 which shows the gradual *in situ* growth of vertically aligned Bi_2S_3 nanorods in the $\text{Cs}_3\text{Bi}_2\text{I}_9$ layer by the spray deposition. These nanorod structures in the composite thin films can be compared to the typical nanorod morphology of the spray-deposited Bi_2S_3 thin film displayed in the figure. Hollow rode-like morphology of Bi_2S_3 by a pulsed ultrasonic spray method was reported elsewhere [36]. In the composite films, the growth of the Bi_2S_3 nanorods is spotted mostly at the grain boundaries of $\text{Cs}_3\text{Bi}_2\text{I}_9$. These nanorods appear denser and larger with the increase in thioacetamide (TA) concentration (0.005–0.05 M noted as TA05 to TA5) as seen in the figure. In the TA5 composite film prepared with the highest thioacetamide concentration, long nanorods protruding from the surface of $\text{Cs}_3\text{Bi}_2\text{I}_9$ can be noticed. The low magnification images in S2 reveal agglomerations on the pCBI thin film because of a non-uniform droplet spreading and solvent evaporation followed by rapid crystallization. On the other hand, the morphology of TA3 composite film presents better uniformity and a smooth surface, supporting the improvement of the thin film formation due to the presence of thioacetamide. Here, thioacetamide may act as a complexing agent in the precursor solution, thereby introducing an additional pyrolysis step in the growth mechanism at the substrate surface.

There have been reports on the synthesis of $\text{Cs}_3\text{Bi}_2\text{I}_9$ precursors by directly mixing CsI and BiI_3 in the stoichiometric ratio in different types of solvents [4,17,37]. In the present case, when the $\text{Cs}_3\text{Bi}_2\text{I}_9$ precursor obtained by mixing CsI and BiI_3 in acetone is sprayed onto the substrate kept at 200 °C, the solvent evaporates resulting in the formation of $\text{Cs}_3\text{Bi}_2\text{I}_9$ thin films with relatively large grains. While using thioacetamide enriched $\text{Cs}_3\text{Bi}_2\text{I}_9$ solution, crystallization of $\text{Cs}_3\text{Bi}_2\text{I}_9$ takes place along with thioacetamide decomposition to sulfur that reacts with bismuth to form Bi_2S_3 at the same temperature. It was reported that Bi ions reacted with thiourea, Bi_2S_3 nanorods [35,36] were formed and the presence of sulfur-enriched precursor controlled the length of the nanorods [38]. In our experiment, the instant evaporation of acetone

results in faster crystallization and coalescence of $\text{Cs}_3\text{Bi}_2\text{I}_9$ limiting the mobility of Bi and S species. Consequently, the formation of Bi_2S_3 is confined to the intergranular region favoring vertical growth leading to aligned nanorods as seen in the morphology analysis. Further studies on the composite thin film growth by varying BiI_3 concentrations and substrate temperatures are needed to understand the detailed mechanism of the nanostructure growth within the bulk of $\text{Cs}_3\text{Bi}_2\text{I}_9$.

The cross-sectional images of pCBI and TA3 film displayed in S2 show enhanced thin composite film growth compared to the pure $\text{Cs}_3\text{Bi}_2\text{I}_9$ film. The cross-section measures 760 nm for pCBI thickness and 1060 nm for TA3 composite film thickness. The simultaneous formation of Bi_2S_3 nanorods may provide nucleation centers for $\text{Cs}_3\text{Bi}_2\text{I}_9$ growth resulting in highly uniform thin films of elongated grains perpendicular to the substrate surface as seen in S3.

3.3. Elemental composition and chemical states

The elemental chemical states and the depth profiling of the composition of pure $\text{Cs}_3\text{Bi}_2\text{I}_9$ and TA3 films were analyzed using XPS. Though a flood gun is used in the measurements for charge compensation, any charging effect was further corrected using the adventitious carbon (C 1s) peak energy at 284.6 eV [17]. The survey spectra of pCBI and TA3 thin films in S4 reveal the presence of Cs, Bi and I in both films. S 2p peaks overlap with Bi 4f peaks, and the intensity of other S peaks is very low to be distinguishable in the TA3 spectrum. Additional peaks corresponding to any other elements are not observed in the survey spectra. Most of the surface contaminants, including adventitious carbon and adsorbed oxygen were removed by the etching process. Fig. 3 shows high resolution XPS spectra of Cs 3d, Bi 4f and I 3d core-levels. The Cs 3 d_{5/2} and 3 d_{3/2} peaks are observed at 724.44 and 738.38 eV for the pCBI thin film whereas for the TA3 composite film, the corresponding peaks are detected at 724.48 and 738.43 eV [7]. The I 3d core level spectra constitute 3d_{5/2} and 3d_{3/2} peaks at 618.93 and 630.43 eV for pCBI thin film and similar values of 618.98 and 630.48 eV for TA3 composite film [7,9]. The Bi 4f high-resolution scan of pCBI thin film in the figure shows the presence of two doublets of Bi 4f_{7/2} and 4f_{5/2}. Hence, Bi 4f was fitted with two doublet pairs, each pair of equal FWHM separated by 5.3 eV, using the Gaussian-Lorentzian sum function and Shirley-type background analysis was done to determine a more accurate peak position and area. For the fitting process, we considered the criteria of preserving the peak area ratio of the doublets (d_{3/2}:d_{5/2} as 0.6,

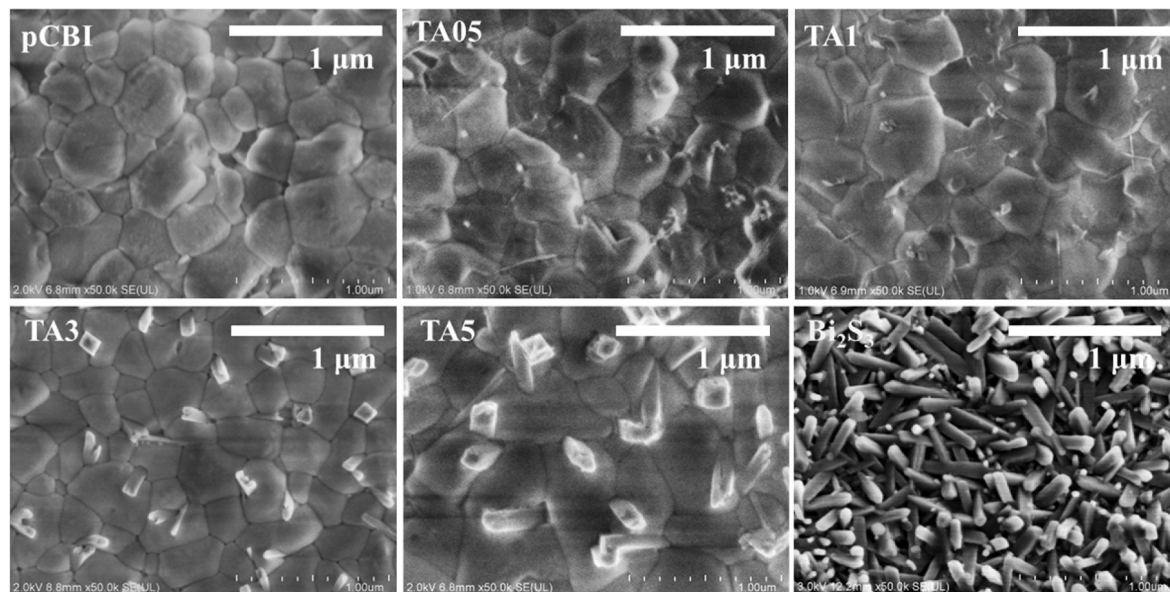


Fig. 2. The SEM images of pure $\text{Cs}_3\text{Bi}_2\text{I}_9$ (pCBI), $\text{Cs}_3\text{Bi}_2\text{I}_9:\text{Bi}_2\text{S}_3$ (TA05, TA1, TA3 and TA5) composite and Bi_2S_3 thin films fabricated by ultrasonic spray deposition.

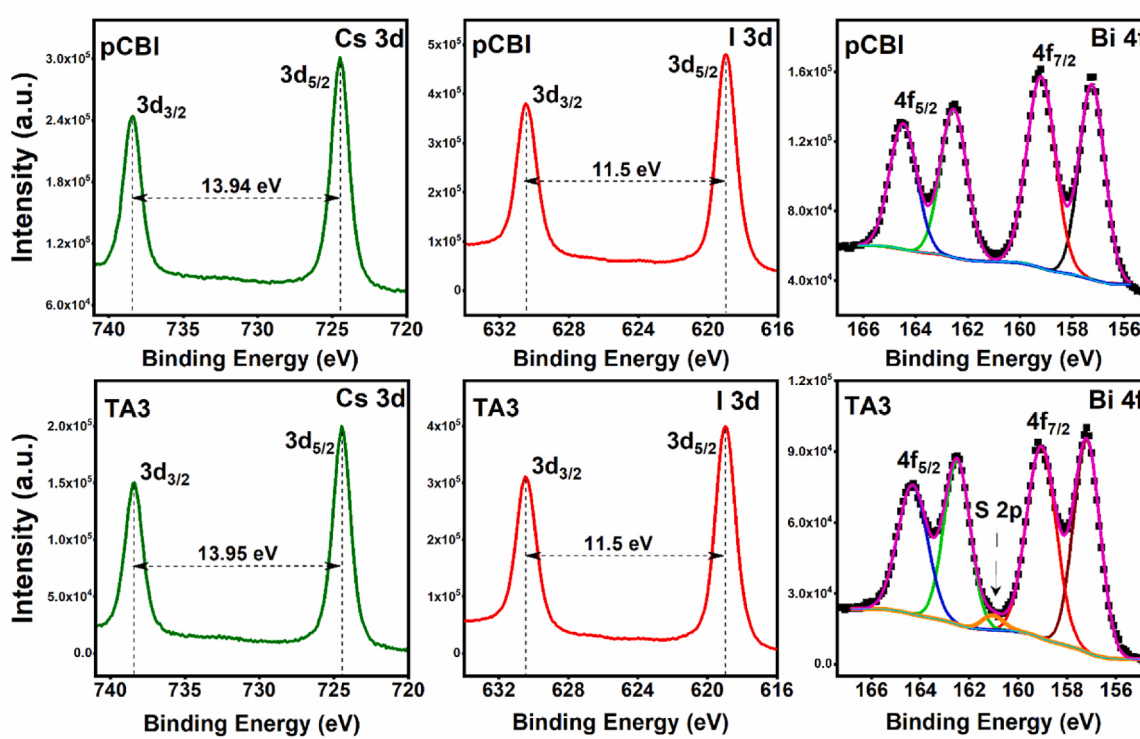


Fig. 3. High-resolution spectra of Cs 3d, I 3d, and Bi 4f core levels in pCBI and TA3 thin films.

$f_{5/2}:f_{7/2}$ as 0.75), and the binding energy separation between the doublets. Bi 4f doublets at 159.18 and 164.48 eV, respectively, are associated with the Bi^{3+} oxidized state in $\text{Cs}_3\text{Bi}_2\text{I}_9$ whereas the peak positions are at 159.10 and 164.40 eV in TA3 composite film [32]. Besides, the 4f doublet near 157.2 and 162.5 eV in both the thin films may be attributed to the atomic bismuth state (Bi^0) due to the etching process to remove the surface layer as reported earlier [7,26]. Additionally, the S 2p peak with small intensity present in the Bi 4f scan of TA3 composite thin film at 161.04 eV is attributed to the S^{2-} state in Bi_2S_3 [35]. The S 2p peak can be compared with that in the high-resolution scan of Bi_2S_3 thin film given in supplementary S5. The intense peaks at 158.28 and 163.58 eV are assigned to the Bi 4f_{7/2} and 4f_{5/2} peaks of the Bi^{3+} state in Bi_2S_3 [36]. Similarly, the peaks observed at 157.08 and 162.38 eV are due to the metallic bismuth (Bi^0) species resulting from the etching process. The shaded peaks of very low intensity at 161.08 and 162.18 eV obtained after the deconvolution are ascribed to the S 2p_{3/2} and 2p_{1/2} peaks, respectively. These peaks correspond to the S^{2-} state in Bi_2S_3 [36].

The sulfur region S 2p (158–168 eV) is composed of spin-orbit coupled S 2p_{1/2} and S 2p_{3/2} separated by 1.16 eV, overlapping with the primary XPS region of Bi 4f (154–168 eV). Also, the sensitivity factor of Bi 4f is 24.83 while that of S 2p is 1.67. Consequently, very high-intensity peaks of Bi 4f suppress the S 2p peaks. The extremely low intensity of other S peaks in the XPS spectrum is indistinguishable.

The binding energy values of all the elements suggest that the presence of nanorods does not change the chemical environment of the $\text{Cs}_3\text{Bi}_2\text{I}_9$ phase. This verifies that the Bi_2S_3 and $\text{Cs}_3\text{Bi}_2\text{I}_9$ are phase-separated with no chemical interactions. The at.% of constituent elements of pCBI calculated using the XPS survey scan as given in supplementary information (S6). The calculations were done by considering the primary doublet peaks of Cs 3d, Bi 4f, and I 3d levels. Comparing the Bi/Cs ratio in both samples, TA3 exhibits a slightly higher value, implying more bismuth content attributed to the presence of Bi_2S_3 , while I/Cs is almost unchanged. A near stoichiometric relation of I/Bi and I/Cs was reported [30] for $\text{Cs}_3\text{Bi}_2\text{I}_9$ thin films deposited on TiO_2 , calculations made using the relative intensities of experimental core levels. In the present study, from the XPS survey scan, a significant deviation from the

stoichiometry can be observed, regarding the I/Bi and I/Cs ratios, while Cs/Bi ratio of nearly 1.1 ($\text{Cs}_3\text{Bi}_2\text{I}_9$) or less for Bi_2S_3 incorporated thin films. Deviation from the stoichiometric ratio can generally be associated with the preferential sputtering effect of Ar + ion etching during XPS analysis [39].

Moreover, the depth profile analysis of the TA3 thin film in S6 shows the elemental distribution from the surface to the TA3/glass substrate interface.

3.4. Optical properties and photoresponse

The films show an onset of absorption around 620 nm with an additional small shoulder around 850 nm as evident from Fig. 1d. The major absorption below 600 nm is due to $\text{Cs}_3\text{Bi}_2\text{I}_9$ which has a band gap of approximately 2.2 eV [3]. The direct band gap values calculated using the Tauc plots (Fig. 1e) are 2.15, 2.21, 2.24, 2.22, and 2.18 eV for pCBI, TA05, TA1, TA3, and TA5 thin films, respectively. The slight increase in the band gap of the TA samples can be ascribed to the lower lattice strain which decreases the width of the valence band and conduction band as reported in the literature [40]. Further, the optical band gap can also be affected by the variations in the crystallite size [41,42]. Therefore, the measured values can be attributed to the combined effect of the changes in the lattice strain and crystallite size, correlating with the XRD results. Also, in the composite thin films, an additional shoulder in the absorption curves around 700–900 nm corresponds to that of the Bi_2S_3 nanorods of the band gap in the range of 1.8–1.37 eV [33,34]. The similar optical band gap values suggest that the *in situ* growth of Bi_2S_3 nanorods has no significant effect on the optical properties of the $\text{Cs}_3\text{Bi}_2\text{I}_9$ phase. However, the small changes in the absorption may be due to changes in the growth or rate of crystallization of $\text{Cs}_3\text{Bi}_2\text{I}_9$ induced by the variation in the thioacetamide concentration.

The photoresponse of the films measured using two symmetric silver electrodes separated by 5 mm on the surface of the thin films is shown in Fig. 4. At a bias of 1 V, TA3 thin film yields a sensitivity of 198 % with a photocurrent up to 1.35 nA while maintaining the low dark current of 0.68 nA compared to pure $\text{Cs}_3\text{Bi}_2\text{I}_9$. From the figure, we can see a

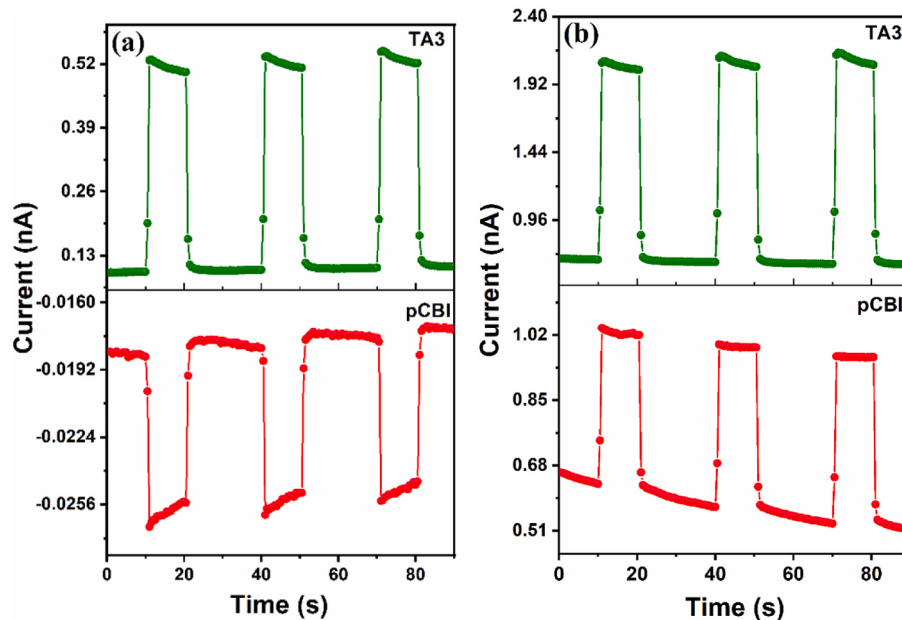


Fig. 4. Photoresponse of the pCBI and TA3 composite thin films under 50 W halogen lamp (a) 0 V and (b) 1 V bias.

negative current in pCBI under zero bias and the current was flipped to positive values by the applied bias (1 V). For the $\text{Cs}_3\text{Bi}_2\text{I}_9:\text{Bi}_2\text{S}_3$ thin films, the dark current and the photoresponse were positive under zero and 1 V bias conditions. The self-driven photoconduction in $\text{Cs}_3\text{Bi}_2\text{I}_9$ thin films might have originated from the ferroelectric properties to generate electrical polarization within the material creating an electric field which, in turn, drives both the dark current and photocurrent similar to bulk photovoltaic effect reported in 2D wide band gap hybrid perovskites [43]. Consequently, the negative current may be due to the direction of the polarization-induced electric field in the pCBI thin films at zero bias. In the case of composite films, the presence of Bi_2S_3 can change the polarization and the resulting field to change the flow of current. The ferroelectric nature of $\text{Cs}_3\text{Bi}_2\text{I}_9$ may be due to the asymmetry of the crystal structure along the c-axis [44]. Recently, a similar effect has also been reported in $\text{Cs}_3\text{Sb}_2\text{I}_9$ films [45]. Further research is required to gain a deeper understanding of the insightful ferroelectric properties exhibited by these materials and the related self-driven photoconduction mechanisms.

The improved photocurrent in the TA3 device is due to the better-photogenerated carrier collection by the Bi_2S_3 nanorods incorporated $\text{Cs}_3\text{Bi}_2\text{I}_9$. The XRD and SEM analysis shows improved crystallite size and surface compactness of TA3 films compared to pCBI, reducing the grain boundaries to improve the charge transport. Besides, the photoactive Bi_2S_3 nanostructures with a lower band gap (1.4 eV) can also contribute to the photon absorption in the composite films. Thus, the TA3 device shows the highest absorption in the UV region and fewer grain boundaries with an optimum density of Bi_2S_3 nanorods. Further, the p- $\text{Cs}_3\text{Bi}_2\text{I}_9$ /n- Bi_2S_3 bulk heterojunctions might have facilitated electric field-induced charge transport resulting in higher current [46,47].

3.5. Thermal stability

TA3 composite thin films were annealed at 200, 300, 350, and 400 °C for 30 min in a low vacuum furnace to analyze the thermal stability and morphological changes. As given in Fig. 5a, the TA3 thin films show an improvement in the (006) growth with annealing temperature. However, at 400 °C the film undergoes decomposition, detecting only CsI peaks in the XRD patterns. However, the Raman spectra in Fig. 5b show an increase in the intensity of the 265 cm^{-1} peak due to Bi_2S_3 . This can be verified by the SEM in Fig. 5c where the film heated at 400 °C

illustrates Bi_2S_3 nanorods and CsI particles.

3.6. Photodetector

Excellent self-powered detection properties were demonstrated by the spray-deposited $\text{Cs}_3\text{Bi}_2\text{I}_9:\text{Bi}_2\text{S}_3$ composite layer compared to the control device using pure $\text{Cs}_3\text{Bi}_2\text{I}_9$ thin film in heterojunction photodetectors. The performance of the two devices can be evaluated from the transient current measurements under AM1.5 illumination. Fig. 6a illustrates the FTO/CdS/ $\text{Cs}_3\text{Bi}_2\text{I}_9/\text{C}-\text{Ag}$ photodetector yielding a continuous fall in the on/off ratio with a notable light-induced photocurrent degradation. As seen in Fig. 6b, the dark current increased from 6.7 nA to 11 nA while the photocurrent reduced from 0.39 μA to 0.27 μA in 10 min due to the light-induced effects which is much more evident in the degrading nature of the curve during illumination. The I-V characteristics of the heterojunction, displayed in Fig. 6c, also indicate the enhanced Schottky nature of the junction under illumination. From the zoomed-in image (inset), zero biased photocurrent is seen. Besides, the unstable response of the device to 405 nm illumination under zero bias is displayed in Fig. 6d.

$\text{Cs}_3\text{Bi}_2\text{I}_9:\text{Bi}_2\text{S}_3$ composite thin film shows better performance in the device structure as illustrated in Fig. 7a (FTO/CdS/TA3/C-Ag). A stabilized photocurrent about four times (~1.8 μA) as that of pure $\text{Cs}_3\text{Bi}_2\text{I}_9$ -based devices was measured under AM1.5 illumination as demonstrated in Fig. 7b. Here, the conducting Bi_2S_3 (S8) nanorods collect the photo-generated carriers before undergoing recombination in the bulk of the $\text{Cs}_3\text{Bi}_2\text{I}_9$ and transfer to the electrodes. More importantly, we can observe an initial increase in photocurrent that stabilized after 200 s without any light-induced degradation and continued to deliver stable dark and photocurrent cycles over 20 min as demonstrated in Fig. 7d. The performance of the self-biased photodetectors with other concentrations was very poor. The TA05 and TA1 films showed a slight improvement compared to that of pure $\text{Cs}_3\text{Bi}_2\text{I}_9$ films. The TA5 film with large Bi_2S_3 nanorods showed very poor performance due to the high roughness and powdery nature of the films. Hence, we chose TA3-based devices for the detailed photodetector studies.

Further, the performance of the composite thin film was evaluated using light sources of 405, 532, 785, 840, 980, and 1064 nm wavelengths with different illumination power at 0 V bias. Here, the 840 and 980 nm illuminations were of 100 mW power and the 405 nm

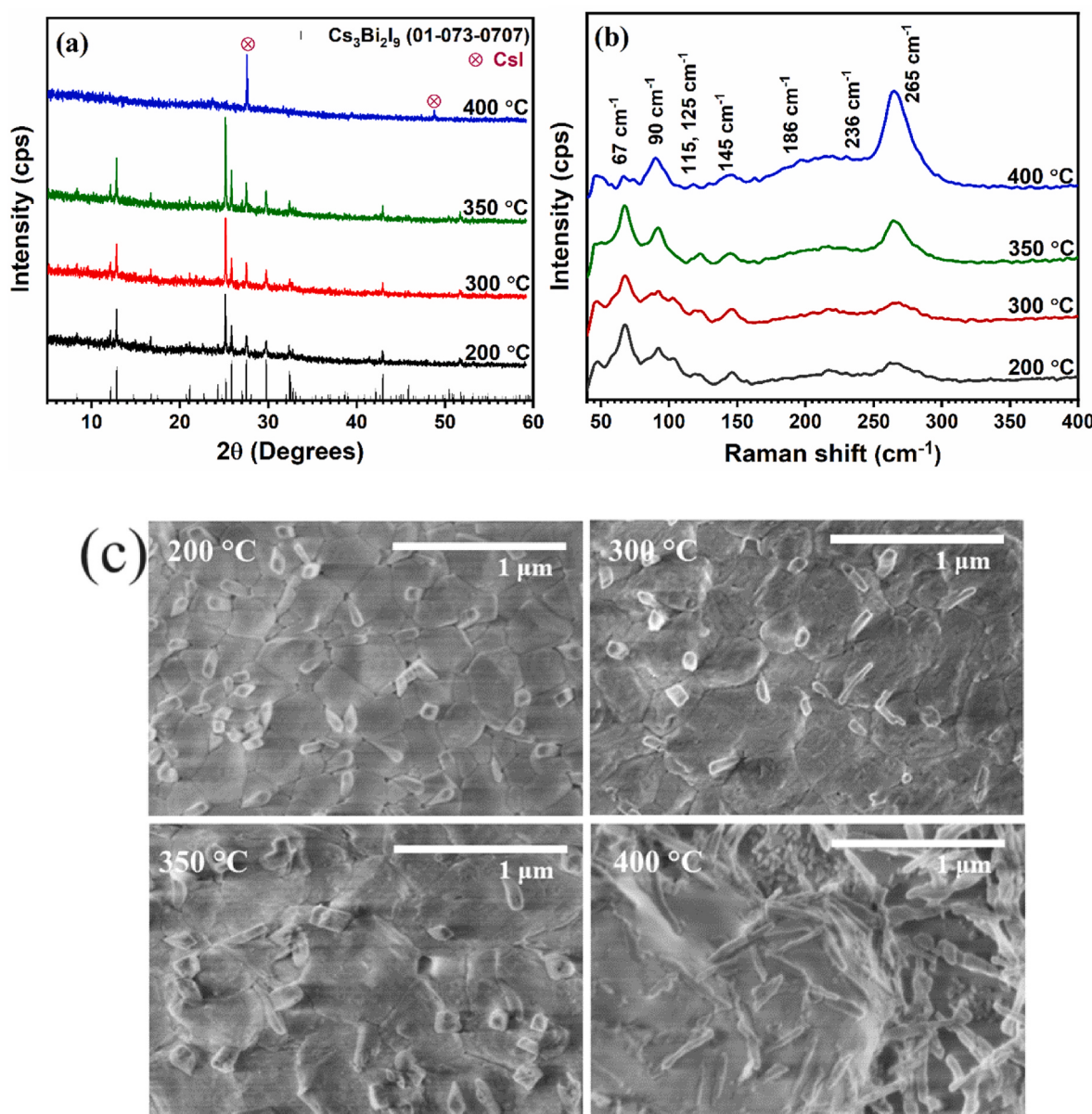


Fig. 5. (a)XRD patterns and (b) Raman spectra of thermally treated TA3 thin films at various temperatures (c)The SEM images of the TA3 composite films with different annealing temperatures.

illumination was of 50 mW power while all other illuminations (532, 785, and 1064 nm) were power-adjustable. The photodetector demonstrated appreciable self-driven response under all the illuminations as seen in Fig. 8 indicating broad detection capabilities of the TA3 composite film, and similar behavior for wavelengths 532, 980, and 1064 nm (Fig. 8 a, c, and d). Fig. 8b shows a sharp increase in photocurrent for 785 nm can be attributed to the fundamental carrier excitation process originating from Bi₂S₃. The Cs₃Bi₂I₉:Bi₂S₃ composite films exhibit a significant onset of absorption in the range of 750–800 nm (Fig. 1d). Also, the absorption spectrum of nanorod-structured Bi₂S₃ thin film illustrates the fundamental absorption edge ~790 nm (S1) and hence Cs₃Bi₂I₉: Bi₂S₃ composite thin films present an anomalous photo-detection curve under 785 nm illumination.

The photodetector delivered maximum photocurrent up to ~0.25 μA under 405 and 532 nm illumination of 50 mW. The dependence of photocurrent on illumination power density as shown in S9a,b was evaluated using the power law ($I_{ph} \propto P^\theta$), displayed in S9c,d, reveals the θ values of 0.95, 0.82, and 0.85 for 532, 785, and 1064 nm lasers,

respectively [12]. The values closer to 1 suggest lower recombination in the Cs₃Bi₂I₉:Bi₂S₃ thin film [24].

The detectivity and responsivity of the TA3 devices are determined for all the illuminations as compared in Fig. 9. In the self-power mode, the TA3 device demonstrated the best detection performance under 532 nm (790 μ Wcm⁻²) photons with a detectivity of 8.18×10^9 Jones and responsivity of 0.59 mA W⁻¹ and the values are comparable with the performance of reported zero biased self-driven photoconduction originated from ferroelectricity of perovskites [43]. The detectivity varied in the broad spectral range of 405–1064 nm from 5.1×10^9 to 6.6×10^7 Jones.

The performance of some of the reported Cs₃Bi₂I₉-based photodetectors is listed in Table 2. The importance of lead-free Cs₃Bi₂I₉ perovskite for photodetection. These literatures encourage further research to improve the properties of Cs₃Bi₂I₉ based photodetectors.

Self-powered photodetectors based on spin-coated Cs₃Bi₂I₉ demonstrated broad spectral response in the 450–950 nm range with detectivities up to $\sim 10^{10}$ – 10^{12} Jones [11]. In the present work, the spray-cast

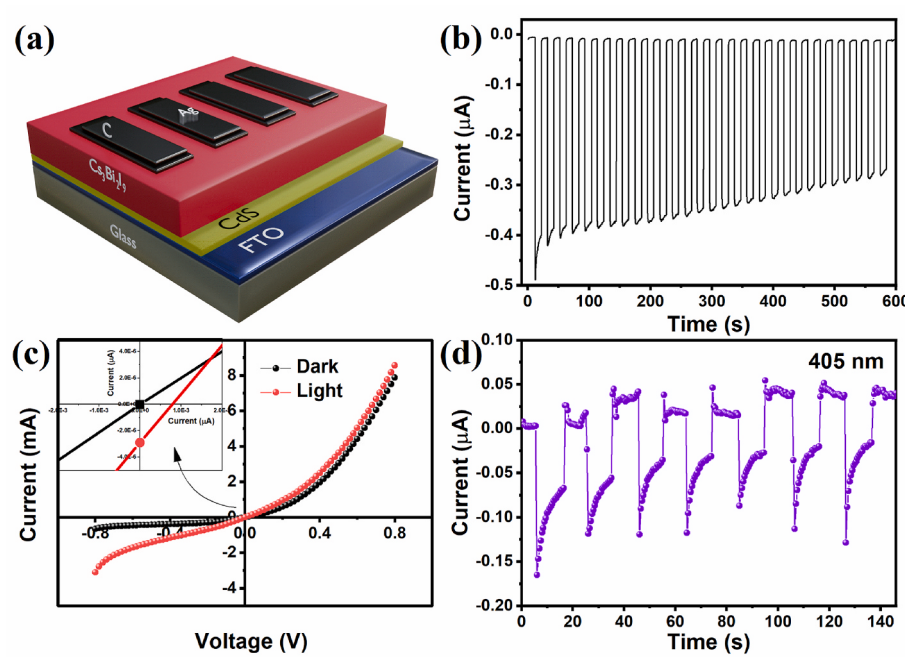


Fig. 6. (a) An illustration of FTO/CdS/pCBI/C-Ag device. (b)The response of the junction under AM 1.5 illumination at 0 V bias and its (c) IV characteristics (inset shows the zoomed in image of 0V) (d) Response of the heterostructure under 405 nm (50 mW) laser illumination.

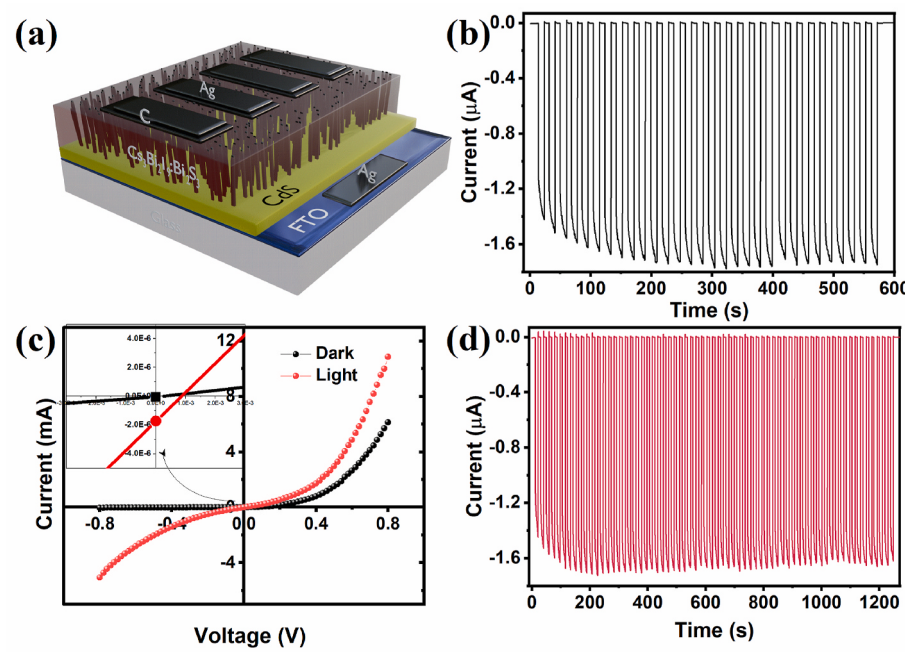


Fig. 7. (a) An illustration of FTO/CdS/TA3/C-Ag device. (b)The response of the device under AM1.5 illumination at 0 V bias (c) The IV characteristics of the heterojunction device (inset shows the zoomed-in image of the graph at 0V) (d) The repeatability and stability of the response under AM1.5 illumination.

device using $\text{Cs}_3\text{Bi}_2\text{I}_9\text{:Bi}_2\text{S}_3$ shows broader detection from the 405–1064 nm wavelength range. More importantly, the photocurrent has been improved to the micro-ampere range without the need for any complicated structure as reported previously using multilayered device configurations using different perovskites [10,13]. Our results obtained with the composite thin films obtained by a single-step ultrasonic spray deposition suggest their potential in various optoelectronic devices for efficient charge extraction and better performance. In our work, the ultrasonic spray deposition technique is used for the simultaneous growth of metal chalcogenide (Bi_2S_3) nanostructures incorporated

cesium bismuth halide perovskite ($\text{Cs}_3\text{Bi}_2\text{I}_9$) using a single precursor solution containing metal halides (CsI and BiI_3) and thioacetamide. This is facilitated by *in-situ* crystallization and growth of the thin films due to thermal energy provided by the substrate heating [19,36]. However, challenges arise in selecting the optimal substrate temperature and solvent for the perovskite: chalcogenide cations balancing the need to optimize the film growth avoiding the formation of impurity phases and preferential loss of volatile components during the spray process. The best approach may involve implementing precursor and solvent engineering techniques to ensure that the reaction takes place exclusively on

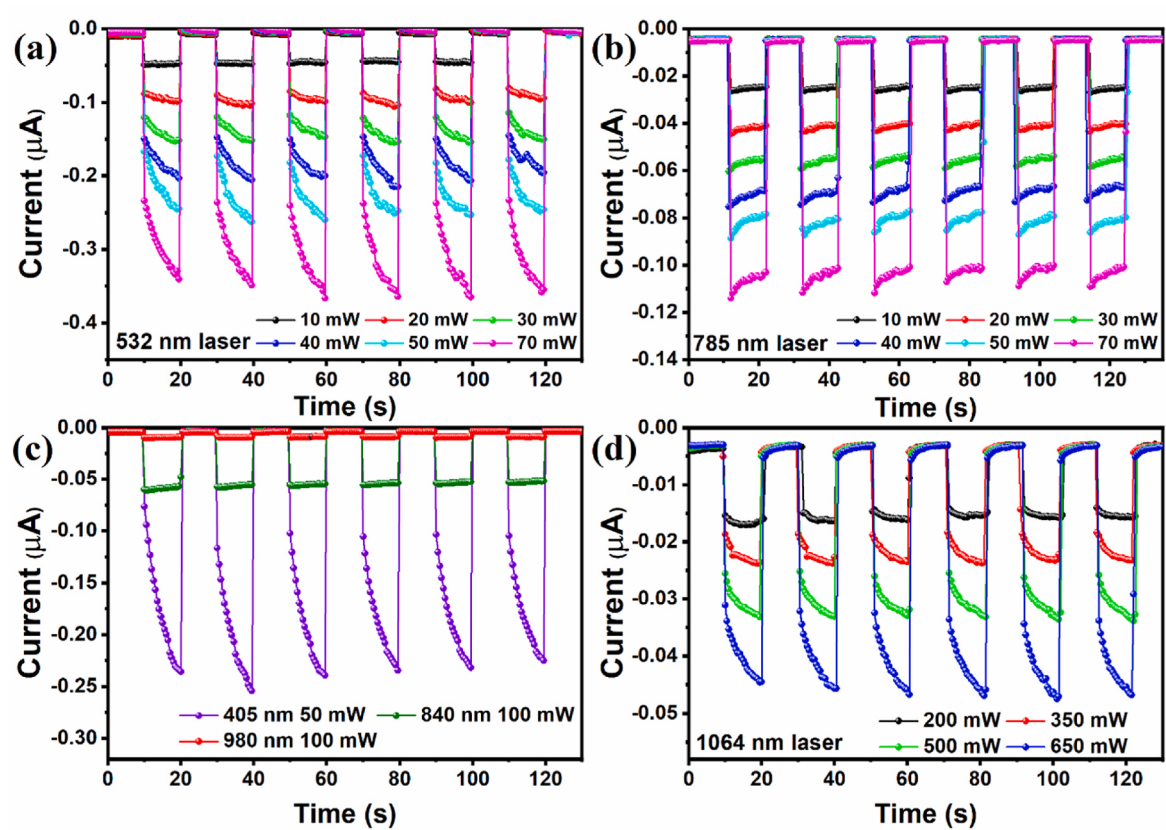


Fig. 8. The response of FTO/CdS/TA3/C-Ag heterostructure to various laser illuminations of (a) 532 nm (b) 785 nm (c) 405, 840, and 980 nm, and (d) 1064 nm laser.

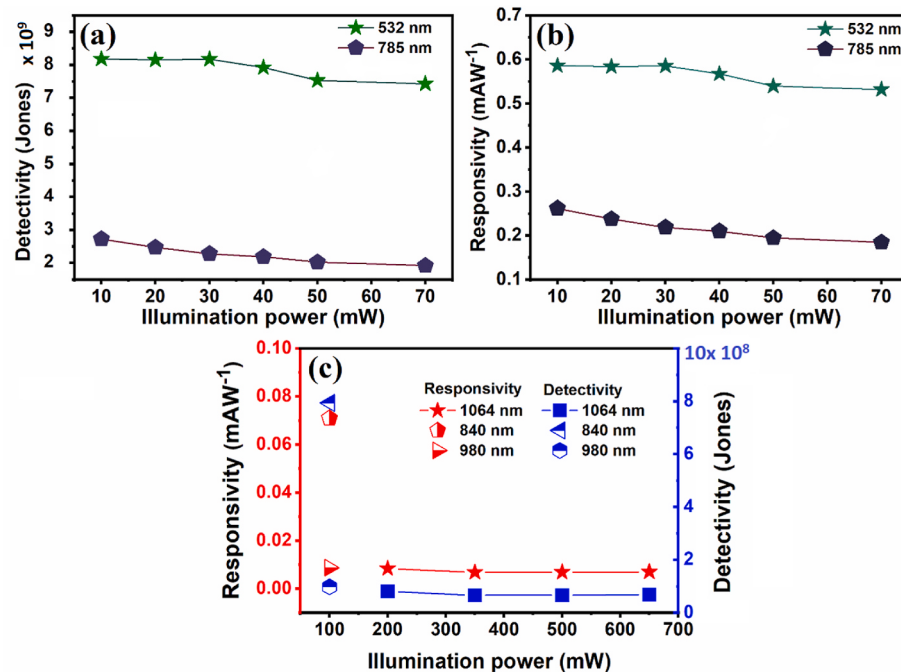


Fig. 9. The detection performance of FTO/CdS/TA3/C-Ag to various illuminations. (a) Detectivity to 532 and 785 (b) Responsivity to 532 and 785 laser illuminations (c) Responsivity and detectivity to 840, 980 and 1064 nm.

the substrates at an appropriate temperature, providing the necessary thermal energy for the complete precursor dissociation [17,19,51,52]. In our experiments, poor device performance can be attributed to the

high surface roughness and the lack of a hole transport layer on the highly resistive $\text{Cs}_3\text{Bi}_2\text{I}_9:\text{Bi}_2\text{S}_3$ composite films. The performance of the spray-deposited composite films in devices can be improved by further

Table 2A comparative analysis of $\text{Cs}_3\text{Bi}_2\text{I}_9$ photodetectors reported in the literature.

Photodetector architecture	Deposition method	Nature of Absorber	$R (\text{AW}^{-1})$	D^* (Jones) ($\times 10^{10}$)	On/off ratio	τ_r/τ_d	Ref.
ITO/Cs ₃ Bi ₂ I ₉ /ITO (450 nm, 10 V)	Spin coating	nanocrystals	33.1×10^{-3}	-1	~40	10.2/37.2	[14]
FTO/Cs ₃ Bi ₂ I ₉ /Ag (white light: 450–950 nm, 0V)	Spin coating	Micro crystals	0.59×10^{-6}	1.2	1.4×10^4	62.74/ 90.25	[11]
ITO/PEDOT:PSS/Cs ₃ Bi ₂ I _{9-x} Br _x /C60/BCP/Ag (410 nm, 0 V)	Spin coating	Thin film	15×10^{-3}	46	4.1×10^4	40.7/27.1	[13]
ITO/Cs ₃ Bi ₂ I ₉ /Au (white light, -2 V)	Space limited method	SC thin film	7.2×10^{-3}	10	1.1×10^4	$247/230 \times 10^{-3}$	[48]
ITO/Cs ₃ Bi ₂ I ₉ /Au (white light, -2 V)	Spin coating	PC thin film	7×10^{-3}	0.72	23–24	$582/385.5 \times 10^{-3}$	[48]
FTO/Al ₂ O ₃ /Cs ₃ Bi ₂ I ₉ /Au (405 nm, 0V)	Spin coating	PC Thin film	100×10^{-3}	-	3.85×10^3 (1.7 mW)	-	[12]
graphene/Cs ₃ Bi ₂ I ₉ (325 nm, -5 V)	Space limited method	Single crystal	13.8×10^{-3}	52.4	-	13.2/15.5	[49]
MoS ₂ /Cs ₃ Bi ₂ I ₉ (325 nm, -5 V)	Space limited method	Single crystal	1.42	1150	-	11.6/14.9	
Ag/Si/Cs ₃ Bi ₂ I ₉ /Au (450 nm, 3 V)	Space limited method	Single crystalline film	-	39	3×10^3	0.0015/0.422	[16]
Au/Cs ₃ Bi ₂ I ₉ /Au (343 nm, 1 V)		Single crystal	3.15×10^{-3}	0.087	-	-	[15]
ITO/SnO ₂ /Cs ₃ Bi ₂ I ₉ -SC/PTAA/Au/ITO (405 nm, 0 V)	SACM	Single crystal	52.06×10^{-3}	100	5.7×10^3	-	[10]
p-Si/Cs ₃ Bi ₂ I ₉ /Graphene (650 nm, -2 V)	Spin coating	nanocrystals	23.6	1750	-	$31/34 \times 10^{-3}$	[50]
FTO/CdS/Cs ₃ Bi ₂ I ₉ :Bi ₂ S ₃ /C/Ag (532, 785 nm, 0 V) Table	Ultrasonic spray	thin film	(0.25–0.6) × 10^{-3}	0.8–0.25	-	-	The present work

optimizing the growth of Bi₂S₃ nanorods and reducing the roughness.

3.7. Conclusions

In summary, the ultrasonic spray deposition technique is efficient in the *in-situ* growth of Bi₂S₃ nanorods in perovskite-inspired Cs₃Bi₂I₉ thin films. We incorporated Bi₂S₃ to improve the photostability of the Cs₃Bi₂I₉ thin film photoconductor and photodiode device. Semiconducting Bi₂S₃ nanorods were effective in collecting the photo-generated carriers from the bulk of the Cs₃Bi₂I₉, thus suppressing the carrier recombination process as well as light and applied electric field-induced degradation of the photocurrent. Also, the lower band edge of the Bi₂S₃ compared to Cs₃Bi₂I₉ suggested photodetection for a wider spectral range of UV–Vis–NIR. The FTO/CdS/Cs₃Bi₂I₉:Bi₂S₃/C–Ag device based on these composite films demonstrated excellent photostability and repeatability in prolonged operations. Under illumination using AM1.5 radiation and zero bias conditions for 100 cycles (20 min of continuous operation), the device of Bi₂S₃ nanorod incorporated Cs₃Bi₂I₉ thin films showed high photostable response compared to that of the pure Cs₃Bi₂I₉ photodetector. The zero-biased photodetector showed broad detection characteristics in the wavelength 405–1064 nm range. Our investigations demonstrate the importance of the ultrasonic spray deposition technique in the *in-situ* growth and control of metal chalcogenide nanostructures in the bulk of metal halide lead-free perovskite thin films.

CRediT authorship contribution statement

Sebin Devasia: Writing – original draft, Validation, Software, Methodology, Investigation, Formal analysis, Data curation. **Sadasivan Shaji:** Writing – review & editing, Validation, Software, Investigation, Funding acquisition, Formal analysis. **David Avellaneda Avellaneda:** Validation, Software, Formal analysis. **Josue Amilcar Aguilar Martinez:** Validation, Software, Formal analysis. **Bindu Krishnan:** Writing – review & editing, Validation, Supervision, Resources, Project administration, Methodology, Investigation, Funding acquisition.

Declaration of competing interest

The authors declare that they have no known competing financial interests or personal relationships that could have appeared to influence the work reported in this paper.

Data availability

Data will be made available on request.

Acknowledgements

The expense of the investigations was covered under the project CB-2016: No- 284800 sanctioned by Consejo Nacional de Humanidad, Ciencia y Tecnología (CONAHCYT), Mexico. One of the authors, Sebin Devasia, acknowledges the doctoral fellowship received from CONAHCYT.

Appendix A. Supplementary data

Supplementary data to this article can be found online at <https://doi.org/10.1016/j.optmat.2024.115532>.

References

- [1] Y. Zhang, Y. Liu, Z. Xu, H. Ye, Z. Yang, J. You, M. Liu, Y. He, M.G. Kanatzidis, S. Liu, Nucleation-controlled growth of superior lead-free perovskite Cs₃Bi₂I₉ single-crystals for high-performance X-ray detection, Nat. Commun. 11 (2020) 2304.
- [2] S. Attique, N. Ali, S. Ali, R. Khatoon, N. Li, A. Khesro, S. Rauf, S. Yang, H. Wu, A potential checkmate to lead: bismuth in organometal halide perovskites, structure, properties, and applications, Adv. Sci. 7 (2020) 1903143.
- [3] N. Ali, X. Wang, S. Rauf, S. Attique, A. Khesro, S. Ali, N. Mushtaq, H. Xiao, C. P. Yang, H. Wu, Enhanced stability in cesium assisted hybrid 2D/3D-perovskite thin films and solar cells prepared in ambient humidity, Sol. Energy 189 (2019) 325–332.
- [4] M.B. Johansson, B. Philippe, A. Banerjee, D. Phuyal, S. Mukherjee, S. Chakraborty, M. Cameau, H. Zhu, R. Ahuja, G. Boschloo, H. Rensmo, E.M.J. Johansson, Cesium bismuth iodide solar cells from systematic molar ratio variation of CsI and BiI₃, Inorg. Chem. 58 (2019) 12040–12052.
- [5] B. Mondal, H.K. Mishra, D. Sengupta, A. Kumar, A. Babu, D. Saini, V. Gupta, D. Mandal, Lead-free perovskite Cs₃Bi₂I₉-derived electroactive PVDF composite-based piezoelectric nanogenerators for physiological signal monitoring and piezo-phototronic-aided strain modulated photodetectors, Langmuir 38 (2022) 12157–12172.
- [6] K. Adams, J. Mallows, T. Li, D. Kampouris, J.H.J. Thijssen, N. Robertson, Cs₃Bi₂I₉ as high-performance electrode material achieving high capacitance and stability in an economical supercapacitor, J. Phys.: Energy 1 (2019) 034001.
- [7] N. Tewari, S.B. Shivarudraiah, J.E. Halpert, Photorechargeable lead-free perovskite lithium-ion batteries using hexagonal Cs₃Bi₂I₉ nanosheets, Nano Lett. 21 (2021) 5578–5585.
- [8] B.-M. Bresolin, P. Sgarbossa, D.W. Bahnemann, M. Sillanpää, Cs₃Bi₂I₉-g-C₃N₄ as a new binary photocatalyst for efficient visible-light photocatalytic processes, Separ. Purif. Technol. 251 (2020) 117320.

- [9] Z.-L. Liu, R.-R. Liu, Y.-F. Mu, Y.-X. Feng, G.-X. Dong, M. Zhang, T.-B. Lu, In situ construction of lead-free perovskite direct Z-scheme heterojunction Cs₃Bi₂I₉/Bi₂WO₆ for efficient photocatalysis of CO₂ reduction, *Sol. RRL* 5 (2021) 2000691.
- [10] K. Dong, H. Zhou, M. Xiao, P. Gui, Z. Gao, F. Yao, W. Shao, C. Liu, C. Tao, W. Ke, G. Fang, Semi-transparent, high-performance lead-free Cs₃Bi₂I₉ single crystal self-driven photodetector, *Appl. Phys. Lett.* 120 (2022).
- [11] A.A. Hussain, Constructing caesium-based lead-free perovskite photodetector enabling self-powered operation with extended spectral response, *ACS Appl. Mater. Interfaces* 12 (2020) 46317–46329.
- [12] W. Li, Y. Liu, Y. Gao, Z. Ji, Y. Fu, C. Zhao, W. Mai, Tunneling-assisted highly sensitive and stable lead-free Cs₃Bi₂I₉ perovskite photodetectors for diffuse reflection imaging, *J. Mater. Chem. C* 9 (2021) 1008–1013.
- [13] D. Liu, B.-B. Yu, M. Liao, Z. Jin, L. Zhou, X. Zhang, F. Wang, H. He, T. Gatti, Z. He, Self-powered and broadband lead-free inorganic perovskite photodetector with high stability, *ACS Appl. Mater. Interfaces* 12 (2020) 30530–30537.
- [14] Z. Qi, X. Fu, T. Yang, D. Li, P. Fan, H. Li, F. Jiang, L. Li, Z. Luo, X. Zhuang, A. Pan, Highly stable lead-free Cs₃Bi₂I₉ perovskite nanoplates for photodetection applications, *Nano Res.* 12 (2019) 1894–1899.
- [15] L. Li, G. Ye, T. Luo, X. Chen, G. Zhang, H. Wu, L. Yang, W. Zhang, H. Chang, Centimeter-sized stable zero-dimensional Cs₃Bi₂I₉ single crystal for mid-infrared lead-free perovskite photodetector, *J. Phys. Chem. C* 126 (2022) 3646–3652.
- [16] Z. Li, X. Liu, C. Zuo, W. Yang, X. Fang, Supersaturation-controlled growth of monolithically integrated lead-free halide perovskite single-crystalline thin film for high-sensitivity photodetectors, *Adv. Mater.* 33 (2021) 210301.
- [17] S. Devasia, S. Shaji, D.A. Avellaneda, J.A. Aguilar Martinez, B. Krishnan, Ultrasonically sprayed Cs₃Bi₂I₉ thin film based self-powered photodetector, *Mater. Chem. Phys.* 296 (2023) 127295.
- [18] J.E. Bishop, J.A. Smith, D.G. Lidzey, Development of spray-coated perovskite solar cells, *ACS Appl. Mater. Interfaces* 12 (2020) 48237–48245.
- [19] X. Feng, Y. He, W. Qu, J. Song, W. Pan, M. Tan, B. Yang, H. Wei, Spray-coated perovskite hemispherical photodetector featuring narrow-band and wide-angle imaging, *Nat. Commun.* 13 (2022) 6106.
- [20] H. Cai, X. Liang, X. Ye, J. Su, J. Guan, J. Yang, Y. Liu, X. Zhou, R. Han, J. Ni, J. Li, J. Zhang, High efficiency over 20% of perovskite solar cells by spray coating via a simple process, *ACS Appl. Energy Mater.* 3 (2020) 9696–9702.
- [21] A. Lojudice, J.K. Cooper, L.H. Hess, T.M. Mattox, I.D. Sharp, R. Buonsanti, Assembly and photocarrier dynamics of heterostructured nanocomposite photoanodes from multicomponent colloidal nanocrystals, *Nano Lett.* 15 (2015) 7347–7354.
- [22] H.-P. Wang, J.-H. He, Toward highly efficient nanostructured solar cells using concurrent electrical and optical design, *Adv. Energy Mater.* 7 (2017) 1602385.
- [23] D.A.A. Leal, S. Shaji, D.A. Avellaneda, J.A.A. Martínez, B. Krishnan, In situ incorporation of laser ablated PbS nanoparticles in CH₃NH₃PbI₃ films by spin-dip coating and the subsequent effects on the planar junction CdS/CH₃NH₃PbI₃ solar cells, *Appl. Surf. Sci.* 508 (2020) 144899.
- [24] F. Cao, L. Meng, M. Wang, W. Tian, L. Li, Gradient energy band driven high-performance self-powered perovskite/CdS photodetector, *Adv. Mater.* 31 (2019) 1806725.
- [25] G. Gonzalez, B. Krishnan, D. Avellaneda, G.A. Castillo, T.K. Das Roy, S. Shaji, Modification of optical and electrical properties of chemical bath deposited CdS using plasma treatments, *Thin Solid Films* 519 (2011) 7587–7591.
- [26] S. Devasia, S. Shaji, D.A. Avellaneda, J.A.A. Martinez, B. Krishnan, In situ crystallization of OD perovskite derivative Cs₃Bi₂I₉ thin films via ultrasonic spray, *J. Alloys Compd.* 893 (2022) 162294.
- [27] G. Greczynski, L. Hultman, X-ray photoelectron spectroscopy: towards reliable binding energy referencing, *Prog. Mater. Sci.* 107 (2020) 100591.
- [28] A.A. Ramachandran, B. Krishnan, S. Devasia, D.A. Avellaneda, M.I. Mendivil Palma, J.A. Aguilar Martinez, S. Shaji, Photosensitive antimony triiodide thin films by rapid iodination of chemically deposited antimony sulfide, *Mater. Res. Bull.* 142 (2021) 111382.
- [29] J.L. Robins, Thin film nucleation and growth kinetics, *Appl. Surf. Sci.* 33–34 (1988) 379–394.
- [30] D. Phuyal, S.M. Jain, B. Philippe, M.B. Johansson, M. Pazoki, J. Kullgren, K. O. Kvashnina, M. Klintenberg, E.M.J. Johansson, S.M. Butorin, O. Karis, H. Rensmo, The electronic structure and band interface of cesium bismuth iodide on a titania heterostructure using hard X-ray spectroscopy, *J. Mater. Chem. A* 6 (2018) 9498–9505.
- [31] A. Nilà, M. Baibarac, A. Matea, R. Mitran, I. Baltog, Exciton–phonon interactions in the Cs₃Bi₂I₉ crystal structure revealed by Raman spectroscopic studies, *Phys. Status Solidi* 254 (2017) 1552805.
- [32] S. Öz, J.-C. Hebig, E. Jung, T. Singh, A. Lepcha, S. Olthof, F. Jan, Y. Gao, R. German, P.H.M. van Loosdrecht, K. Meerholz, T. Kirchartz, S. Mathur, Zero-dimensional (CH₃NH₃)₃Bi₂I₉ perovskite for optoelectronic applications, *Sol. Energy Mater. Sol. Cell.* 158 (2016) 195–201.
- [33] H. Song, X. Zhan, D. Li, Y. Zhou, B. Yang, K. Zeng, J. Zhong, X. Miao, J. Tang, Rapid thermal evaporation of Bi₂S₃ layer for thin film photovoltaics, *Sol. Energy Mater. Sol. Cell.* 146 (2016) 1–7.
- [34] H. Bao, X. Cui, C.M. Li, Y. Gan, J. Zhang, J. Guo, Photoswitchable semiconductor bismuth sulfide (Bi₂S₃) nanowires and their self-supported nanowire arrays, *J. Phys. Chem. C* 111 (2007) 12279–12283.
- [35] A. Moyssewicz, Scalable one-pot synthesis of bismuth sulfide nanorods as an electrode active material for energy storage applications, *J. Solid State Electrochem.* 23 (2019) 1191–1199.
- [36] S.-Y. Wang, Y.-W. Du, Preparation of nanocrystalline bismuth sulfide thin films by asynchronous-pulse ultrasonic spray pyrolysis technique, *J. Cryst. Growth* 236 (2002) 627–634.
- [37] R. Waykar, A. Bhorde, S. Nair, S. Pandharkar, B. Gabhale, R. Aher, S. Rondiya, A. Waghmare, V. Doiphode, A. Punde, P. Vairale, M. Prasad, S. Jadkar, Environmentally stable lead-free cesium bismuth iodide (Cs₃Bi₂I₉) perovskite: synthesis to solar cell application, *J. Phys. Chem. Solid.* 146 (2020) 109608.
- [38] M.B. Sigman, B.A. Korgel, Solventless synthesis of Bi₂S₃ (Bismuthinite) nanorods, Nanowires, and Nanofabric, *Chem. Mater.* 17 (2005) 1655–1660.
- [39] J.B. Malherbe, R.Q. Odendaal, Ion sputtering, surface topography, SPM and surface analysis of electronic materials, *Appl. Surf. Sci.* 144–145 (1999) 192–200.
- [40] M. Zargarpour, F. Jamali-Sheini, M. Cheraghizade, Sonochemical synthesis of Fe-doped Cu₃Se₂ nanoparticles: correlation of the strain and electrical properties for optoelectronics applications, *Adv. Powder Technol.* 32 (2021) 3412–3424.
- [41] M. Cheraghizade, F. Jamali-Sheini, Space-charge-limited current activation in self-powered and solar-range nanostructured Cu₃Se₂ photodetector by Zn concentrations, *Opt. Mater.* (2023).
- [42] N. Tabrizi, F. Jamali-Sheini, S. Ebrahimiasl, M. Cheraghizade, Enhanced self-powered and visible-range photodetector performance of Ag₂S nanostructures by Cu concentrations, *Sensor Actuator Phys.* 358 (2023) 114436.
- [43] C. Ji, D. Dey, Y. Peng, X. Liu, L. Li, J. Luo, Ferroelectricity-driven self-powered ultraviolet photodetection with strong polarization sensitivity in a two-dimensional halide hybrid perovskite, *Angew. Chem. Int. Ed.* 59 (2020) 18933–18937.
- [44] J. Liang, Q. Fang, H. Wang, R. Xu, S. Jia, Y. Guan, Q. Ai, G. Gao, H. Guo, K. Shen, X. Wen, T. Terlier, G.P. Wiederrecht, X. Qian, H. Zhu, J. Lou, Perovskite-Derivative valleytronics, *Adv. Mater.* 32 (2020) 2004111.
- [45] V.P.V. Sasidharan, M.U.R. Hernandez, S. Shaji, D.A. Avellaneda, S.K. Chandran, M. G. Méndez, B. Krishnan, Cesium antimony iodide perovskite thin films by rapid iodization of Sb₂S₃-CsCl precursor under ambient conditions, *J. Alloys Compd.* 972 (2024) 172870.
- [46] M. Zamani, F. Jamali-Sheini, M. Cheraghizade, Visible-range and self-powered bilayer p-Si/n-Bi₂S₃ heterojunction photodetector: the effect of Au buffer layer on the optoelectronics performance, *J. Alloys Compd.* 905 (2022) 164119.
- [47] M. Zamani, F. Jamali-Sheini, M. Cheraghizade, Space-charge-limited current passivation of the self-powered and ultraviolet-to-visible range bilayer p-Si/n-Bi₂S₃ heterojunction photodetector by Ag coating, *J. Alloys Compd.* 933 (2023) 167665.
- [48] W.-G. Li, X.-D. Wang, J.-F. Liao, Y. Jiang, D.-B. Kuang, Enhanced on-off ratio photodetectors based on lead-free Cs₃Bi₂I₉ single crystal thin films, *Adv. Funct. Mater.* 30 (2020) 1909701.
- [49] P. Zhang, Y. Zhang, W. Wang, L. Gao, G. Li, S. Zhang, J. Lu, Y. Yu, J. Zhang, Multispectral photodetectors based on 2D material/Cs₃Bi₂I₉ heterostructures with high detectivity, *Nanotechnology* 32 (2021) 415202.
- [50] J. Wang, Y. Li, L. Ma, G. Shen, Q. Yang, Air-stabilized lead-free hexagonal Cs₃Bi₂I₉ nanocrystals for ultrahigh-performance optical detection, *Adv. Funct. Mater.* 32 (2022) 2203072.
- [51] L.Y. Kupriyanov, Chapter 4 - application of semiconductor sensors in experimental investigation of physical – chemical processes, in: L.Y. Kupriyanov (Ed.), *Handbook of Sensors and Actuators*, Elsevier Science B.V., 1996, pp. 219–279.
- [52] M. Bouachri, M. Oubakalla, H. El Farri, C. Díaz-Guerra, J. Mhalla, J. Zimou, A. El-Habib, M. Bereich, K. Nouneh, M. Fahoume, P. Fernández, A. Quannou, Substrate temperature effects on the structural, morphological and optical properties of Bi₂S₃ thin films deposited by spray pyrolysis: an experimental and first-principles study, *Opt. Mater.* 135 (2023) 113215.